

Solar-sail control laws for perturbed Earth-bound trajectories

Carzana, L.; Visser, P.N.A.M.; Heiligers, M.J.

Publication date

2021

Document Version

Final published version

Published in

72nd International Astronautical Conference

Citation (APA)

Carzana, L., Visser, P. N. A. M., & Heiligers, M. J. (2021). Solar-sail control laws for perturbed Earth-bound trajectories. In *72nd International Astronautical Conference* Article IAC-21-C1.3.5

Important note

To cite this publication, please use the final published version (if applicable).
Please check the document version above.

Copyright

Other than for strictly personal use, it is not permitted to download, forward or distribute the text or part of it, without the consent of the author(s) and/or copyright holder(s), unless the work is under an open content license such as Creative Commons.

Takedown policy

Please contact us and provide details if you believe this document breaches copyrights.
We will remove access to the work immediately and investigate your claim.

Solar-sail control laws for perturbed Earth-bound trajectories

Livio Carzana^{a*}, Pieter Visser^a, Jeannette Heiligers^a

^a Faculty of Aerospace Engineering, Delft University of Technology, Kluyverweg 1, Delft, The Netherlands 2629 HS

* Corresponding Author

Abstract

Solar sailing is a spacecraft propulsion method relying solely on solar radiation pressure to provide thrust and is therefore propellantless by nature. Although it represents a practical and promising propulsion system particularly suited for heliocentric flight regimes, near-term sailcraft missions will remain Earth-bound due to the current technology readiness level. This paper aims to show the suitability of solar sailing for planetocentric applications for future Earth-bound solar-sail missions. In Earth orbit, the sailcraft is subjected to perturbations absent or negligible in heliocentric flight, including the effect of eclipses, non-spherical gravity and aerodynamic drag. The magnitude of these perturbations can be comparable to, or even exceed that of solar radiation pressure and their effect on the solar-sail dynamics should be investigated to ensure the sailcraft's transfer capabilities and controllability. This paper does so by including the gravitational and aerodynamic perturbations in the optimal control problem. From this formulation, steering laws can be derived to optimally change individual orbital elements. These newly derived steering laws form an extension to the laws found by McInnes for unperturbed solar-sail Earth-bound motion. By accounting for the perturbations in the derivation of the steering laws, their effect can be exploited by the sailcraft to achieve orbits otherwise unreachable. The improved maneuverability will be quantified based on the established increase of the targeted orbital element. A range of different starting orbits will be considered to characterize how the perturbations affect the solar-sail maneuvering capabilities in different orbital regimes. As demonstration of the real need for this investigation, NASA's Advanced Composite Solar Sail System (ACS3) mission will be considered as real-case scenario. This mission is scheduled for launch in mid-2022 and may benefit from the steering laws derived in this paper to proof the maneuverability of solar sails in Earth orbit.

Keywords: solar sail, trajectory optimization, steering law, Earth-bound, aerodynamic drag, ACS3 mission

1. Introduction

The usage of solar sails as main propulsion system for spaceflight applications is an idea that was first investigated at the beginning of the last century and has since drawn increasingly more attention worldwide [1]. The research interest in solar sailing, initially within the scientific community and later also within space agencies, is mainly driven by its propellantless nature. In the last decades many studies on solar sailing demonstrated its applicability to a wide variety of mission scenarios, ranging from interplanetary and interstellar missions to planet-centered ones [2]. Analyses of solar-sail interplanetary and deep-space trajectories have clearly shown the mission-enabling potential of solar sails and, in particular, the promising thrusting capabilities when approaching the inner Solar System, where solar radiation pressure (SRP) is particularly strong and an improved sailcraft maneuverability is achieved [2,3]. While the majority of research works indeed focused on interplanetary solar-sail mission applications, most solar-sail missions launched to date have flown solely in low Earth orbit (LEO). Their purpose was to either show the feasibility of solar-sail de-orbiting (e.g., NASA's NanoSail-D2 mission [4]), the successful control of SRP as propulsive means, or the advancements in sail manufacturing and deployment

capabilities (e.g., The Planetary Society's LightSail 1 and LightSail 2 [5,6]). In a similar fashion, other near-future solar-sail missions – such as NASA's Advanced Composite Solar Sail System (ACS3) mission – are also expected to be launched in LEO and act as sail technology and orbit control demonstrators [7].

Although solar-sail technology demonstrators have been flown mostly in LEO, thus far the research conducted on planetocentric solar-sail orbital dynamics is limited. Most of the studies on the topic are based on the solar-sail control laws first devised by McInnes [1], valid for simplistic, perfectly-reflecting solar sails with either unperturbed two-body problem (2BP) dynamics or gravitational perturbations only. Applications of such control laws range from the analysis of planetocentric solar-sail trajectories [8] to the study of Earth-escape strategies [9]. When considering also non-gravitational perturbations in the analysis of Earth-bound solar-sail trajectories an increased degree of complexity is achieved, which stems from the highly nonlinear dynamics to be considered. Indeed, perturbing accelerations such as the planetary radiation pressure and aerodynamic accelerations can achieve magnitudes comparable to – or even greater than – the SRP acceleration, therefore making the dynamics deviate substantially from the ones of the 2BP with ideal SRP

acceleration. As a consequence, results found with the latter dynamics have limited applicability in the analysis of high-fidelity solar-sail trajectories. In addition, the resulting highly nonlinear dynamical models considering the effects of planetary radiation pressure and/or aerodynamics significantly complicate the computation of optimal steering laws. Preliminary studies on perturbed, Earth-bound sailcraft trajectories have been proposed only in small numbers, with particular focus on the analysis of the coupled effects of SRP and planetary radiation pressure for Earth-centered orbits [10] and studies on SRP and aerodynamics-based optimal control laws for orbit raising and maneuvering [11,12,13]. However, due to the complexity of finding such steering laws in a highly perturbed environment, the methods and results proposed are valid only under simplifying assumptions (e.g., on the orbit shape and its orientation with respect to the Sun's position) and for orbit raising and inclination change steering laws only.

This paper proposes a novel technique to efficiently and accurately optimize Earth-bound solar-sail trajectories in the presence of SRP, gravitational perturbations, and aerodynamic drag. Unlike all other methods employed to date to solve this optimization problem, the one proposed here can be used for any steering law and applied to any orbital regime. This first-of-its-kind technique is based on the idea of pre-solving the optimization problem for a wide set of conditions and to interpolate the optimal solutions found during the trajectory propagation. In this work, this optimization technique is described in its entirety, with focus on its accuracy and limited runtime. NASA's upcoming ACS3 mission is taken as a specific and realistic test case. The ACS3 mission will be launched into a 715 km altitude Sun-synchronous orbit. The results in this paper will demonstrate the sailcraft's ability to change its orbital

altitude and inclination. However, also more generic analyses on applicable steering laws and orbital altitudes are provided, though limited to Sun-synchronous orbits. This class of orbits is selected to reduce the design space, justified by the fact that this class is often used for Earth-centered scientific missions. Nevertheless, the designed novel optimization method presented in this work is applicable to any steering law and orbital regime. Hence, this paper significantly contributes to the body of knowledge on optimal solar-sail controls laws in the near-Earth environment.

2. Dynamical Model

In this section the dynamical model used throughout this paper is presented. First, different reference frames and coordinate systems are defined and subsequently the sailcraft equations of motion (EoM) are given.

2.1 Reference Frames and Coordinate Systems

In the following sections, different reference frames and coordinate systems are presented to conveniently express the sailcraft dynamics and optimization problem under investigation.

2.1.1 Earth-centered Inertial Reference Frame

The Earth-centered inertial (ECI) reference frame is the frame in which the sailcraft EoM are propagated. This Cartesian frame is indicated by $O_I(\hat{x}_I, \hat{y}_I, \hat{z}_I)$ and is centered in the Earth's center of mass, with the \hat{x}_I -axis pointing towards the mean vernal equinox at January 1st, 2000, the \hat{z}_I -axis pointing perpendicular to the mean equatorial plane at January 1st, 2000 (towards the Northern hemisphere), and the \hat{y}_I -axis completes the right-handed frame.

2.1.2 Sunlight Reference Frame

The sunlight reference frame is a sailcraft-centered frame indicated by $O_S(\hat{x}_S, \hat{y}_S, \hat{z}_S)$ and illustrated in Fig. 1. The \hat{x}_S -axis points in the Sun-to-sailcraft direction (i.e., parallel to the direction of sunlight), $\hat{y}_S = \hat{z}_I \times \hat{x}_S$, and the \hat{z}_S -axis completes the right-handed frame. Since a flat solar-sail model is considered in this work, the sailcraft orientation is uniquely determined by the sail normal direction, \hat{n} , which can be defined by two attitude angles: the cone angle α , defined as the angle between the direction of sunlight, \hat{x}_S , and the sail normal direction, \hat{n} , and the clock angle δ , measured from the \hat{z}_S direction to the projection of the sail normal onto the (\hat{y}_S, \hat{z}_S) plane (see Fig. 1). Commonly, only one side of the solar sail can be exposed to direct sunlight. Hence, in this paper it is assumed that the sail normal never has a component pointing towards the Sun's hemisphere, i.e., $\alpha \in [0, \pi/2]$ and $\delta \in [0, 2\pi]$. The sail normal expressed in the sunlight frame, \hat{n}_S , is then found as:

$$\hat{n}_S = \cos \alpha \hat{x}_S + \sin \alpha \sin \delta \hat{y}_S + \sin \alpha \cos \delta \hat{z}_S \quad (1)$$

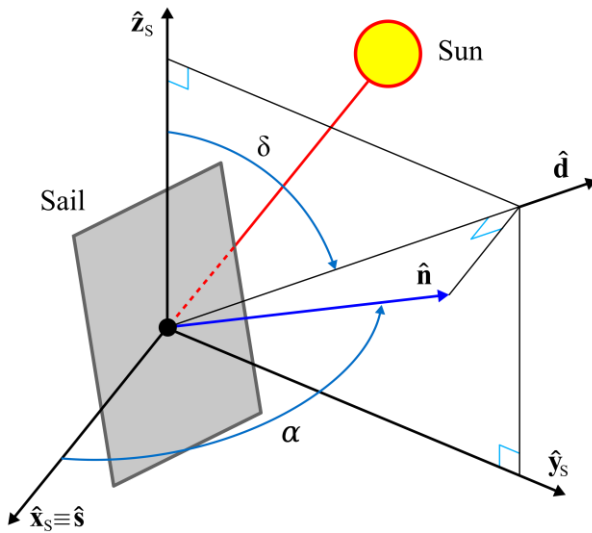


Fig. 1. Sailcraft normal direction and attitude angles in the sunlight reference frame.

2.1.3 Velocity Reference Frame

The velocity reference frame $O_V(\hat{x}_V, \hat{y}_V, \hat{z}_V)$ illustrated in Fig. 2 is centered in the sailcraft and has its \hat{x}_V -axis pointing along the direction of the inertial velocity, \hat{v} , the \hat{z}_V -axis parallel to the satellite's orbital momentum vector, \hat{h} , and the \hat{y}_V -axis such that it forms a right-handed frame. In the frame $O_V(\hat{x}_V, \hat{y}_V, \hat{z}_V)$ the sail normal direction is uniquely identified by the angular coordinates ξ , χ , and ζ shown in Fig. 2. These variables are correlated as:

$$\cos \zeta = \cos \xi \cos \chi \quad (2)$$

The range for each of these angles depends on the instantaneous position of the Sun with respect to the sailcraft, in agreement with the assumption that the sail normal direction always has a component pointing away from the Sun. Using these angular coordinates and Eq. (2), the sail normal direction expressed in the velocity frame, \hat{n}_V , is defined as:

$$\hat{n}_V = \cos \zeta \hat{x}_V + \cos \chi \sin \xi \hat{y}_V + \sin \chi \hat{z}_V \quad (3)$$

Fig. 2 also illustrates the aerodynamic drag direction, \hat{D} , and lift direction, \hat{L} : the first is always opposite to \hat{v} , while the latter points either parallel or antiparallel to the projection of \hat{n} onto the (\hat{x}_V, \hat{z}_V) plane, as expressed by the following relation:

$$\hat{L} = -\text{sign}(\cos \zeta) \frac{\cos \chi \sin \xi \hat{y}_V + \sin \chi \hat{z}_V}{\|\cos \chi \sin \xi \hat{y}_V + \sin \chi \hat{z}_V\|} \quad (4)$$

In Eq. (4) the minus sign guarantees that $\hat{n}_V \cdot \hat{L} \leq 0$ (which should always hold true for a flat plate), while the "sign" function takes into account the aerodynamic symmetry of the flat sail and ensures that the lift direction corresponding to the sail normal directions \hat{n} and $-\hat{n}$ is the same. Ultimately, it is worth noting that due to the

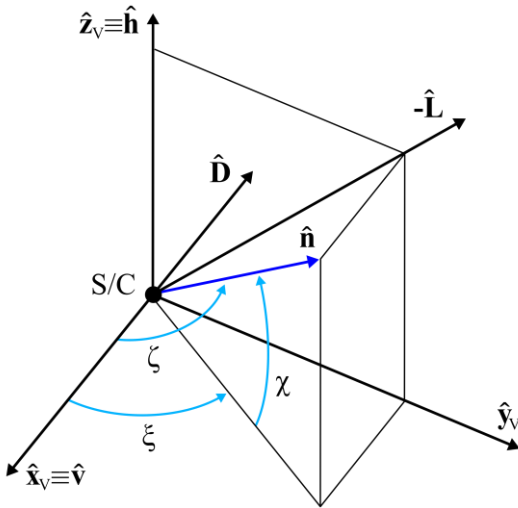


Fig. 2. Sailcraft attitude angles and aerodynamic drag, lift, and sail normal directions in the velocity reference frame.

aerodynamic symmetry the directions \hat{v} , \hat{n} , \hat{L} , and \hat{D} all lie in the same plane.

2.1.4 Optimization Reference Frame

The optimization reference frame $O_O(\hat{x}_O, \hat{y}_O, \hat{z}_O)$ depicted in Fig. 3 is centered in the sailcraft and defined such that its \hat{x}_O -axis points in the drag direction, \hat{D} , the \hat{z}_O -axis points along $\hat{z}_O = (\hat{D} \times \hat{s})$, and the \hat{y}_O -axis completes the right-handed frame. The angle $\eta \in [0, \pi]$ is measured from the drag direction to the sunlight direction, so that the following relation holds:

$$\eta = \cos^{-1}(\hat{D} \cdot \hat{s}) \quad (5)$$

Within this reference frame, the sail normal direction, \hat{n}_O , can be expressed in a similar fashion to Eq. (1) as:

$$\hat{n}_O = \cos \zeta \hat{x}_O + \sin \zeta \sin \gamma \hat{y}_O + \sin \zeta \cos \gamma \hat{z}_O \quad (6)$$

where $\zeta \in [0, \pi]$ represents the angle between the \hat{x}_O direction and the sail normal direction, \hat{n} , and $\gamma \in [0, 2\pi]$ is the angle measured from the \hat{z}_O direction to the projection of the sail normal onto the (\hat{y}_S, \hat{z}_S) plane. These angles can be visualized through Fig. 1 by substituting the sunlight frame axes, \hat{x}_S , \hat{y}_S , and \hat{z}_S , with the optimization frame axes, \hat{x}_O , \hat{y}_O , and \hat{z}_O , and by substituting the angles α and δ with ζ and γ .

2.2 Equations of Motion

In this paper, the solar sail is assumed to be Earth-bound and its motion is determined by the SRP, aerodynamic, and gravitational accelerations. Its EoM are defined in the ECI frame and take the following form:

$$\ddot{\mathbf{r}} + \frac{\mu_{\oplus}}{r^3} \mathbf{r} = \mathbf{a}_{SRP}(\mathbf{u}(t)) + \mathbf{a}_{aero}(\mathbf{u}(t)) + \mathbf{a}_{J2} \quad (7)$$

where the dot notation is used to indicate differentiation with respect to time t and $\mu_{\oplus} = 398600.4415 \text{ km}^3/\text{s}^2$ is the Earth's gravitational parameter [14]. The vectors \mathbf{r} and \mathbf{a} represent the sailcraft position and acceleration vectors in the ECI frame, respectively, while $\mathbf{u}(t) = \hat{n}_I(t)$ is the sailcraft control vector equal to the inertial sail normal direction. The subscripts "SRP" and "aero"

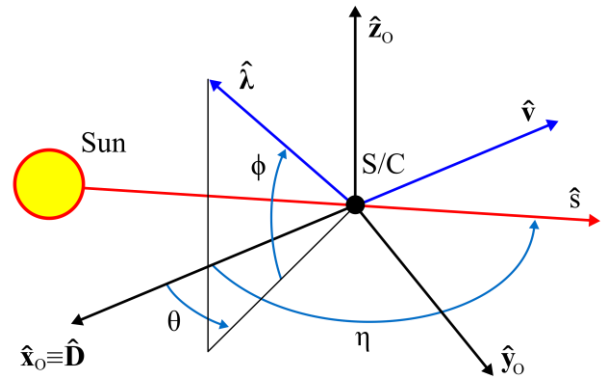


Fig. 3. Optimization reference frame.

refer to the SRP and aerodynamic accelerations, respectively, while “J2” indicates the gravitational perturbing acceleration due to the non-spherical, oblate shape of the Earth, modeled through the J_2 spherical harmonics coefficient. By providing an initial time, t_0 , an initial sailcraft state, $\mathbf{X}_0 = \mathbf{X}(t_0)$, and the control law $\mathbf{u}(t)$, Eq. (7) can be used to propagate the solar-sail state vector $\mathbf{X}(t)$ and find the sailcraft trajectory. The above-mentioned accelerations used to determine the EoM are described in more detail in the following sections.

2.2.1 Solar Radiation Pressure Acceleration

The SRP acceleration model used in this work assumes the solar sail to behave as a flat, perfectly reflecting surface. When adopting this sail model, hereinafter referred to as “ideal”, the SRP acceleration becomes a function of the sailcraft attitude only and can be conveniently expressed in the sail-fixed reference frame O_S as [1]:

$$\mathbf{a}_{SRP,S} = \nu a_c \cos^2 \alpha \hat{\mathbf{n}}_S \quad (8)$$

where $\nu \in [0,1]$ is the shadow factor and a_c denotes the sailcraft characteristic acceleration defined as [1]:

$$a_c = 2S_{\oplus}/c\sigma \quad (9)$$

with $S_{\oplus} = 1367 \text{ W/m}^2$ equal to the solar flux at a distance of 1 AU from the Sun [14], $c = 299792458 \text{ m/s}$ representing the speed of light [14], and σ the solar-sail loading parameter, equal to the ratio of the sailcraft total mass to its sail surface area. The shadow factor ν in Eq. (8) takes into account the effect of eclipses and its value ranges from 0 (no sunlight reaching the sail) to 1 (sail completely illuminated). In this paper, eclipses are modeled with a conical shadow model similar to the one presented in [15] and [16], with the only difference that penumbra is treated as umbra. This means that $\nu = 0$ not only when the sailcraft is in the Earth’s umbra, but also when in penumbra, thus leading to more conservative results. The Earth radius considered for this conical shadow model is $R_{\oplus} = 6378.1363 \text{ km}$ [14].

Based on Eq. (8), the expression of the SRP acceleration in the O_I frame is:

$$\mathbf{a}_{SRP,I} = \nu a_c \cos^2 \alpha \hat{\mathbf{n}}_I \quad (10)$$

with

$$\hat{\mathbf{n}}_I = R_{S \rightarrow I} \cdot \hat{\mathbf{n}}_S \quad (11)$$

where $R_{S \rightarrow I}$ is the rotation matrix to transform vectors from the O_S frame to the O_I frame, which depends on the sailcraft position and time.

2.2.2 Aerodynamic Acceleration

Similar to the SRP acceleration, the aerodynamic acceleration is also modeled assuming the solar sail to be a flat plate. By making the additional assumption that the sailcraft velocity is much larger than the thermal velocity of the atmospheric particles, the hyperthermal free-molecular flow model presented in [17] can be used to describe the sail aerodynamics. Such model has already been employed in [11] and [13] to analyze solar-sail trajectories in the presence of atmospheric drag and is based on the following expression for the aerodynamic acceleration in the O_V frame [13]:

$$\mathbf{a}_{aero,V} = \mathbf{D} + \mathbf{L} = (C_D \hat{\mathbf{D}} + C_L \hat{\mathbf{L}}) \rho v^2 / 2\sigma \quad (12)$$

In Eq. (12), ρ represents the atmospheric density, v the magnitude of the sailcraft inertial velocity, and C_D and C_L the drag and lift coefficients defined as [13]:

$$C_D = 2[\sigma_T + \sigma_N V_R |\cos \zeta| + (2 - \sigma_N - \sigma_T) \cos^2 \zeta] |\cos \zeta| \quad (13)$$

$$C_L = 2[\sigma_N V_R + (2 - \sigma_N - \sigma_T) |\cos \zeta|] |\cos \zeta| \sin \zeta \quad (14)$$

where σ_N and σ_T represent the normal and tangential momentum accommodation coefficients, respectively, and V_R is the ratio of the atmospheric particle average thermal velocity to the sailcraft inertial velocity. Based on [18], this paper uses: $\sigma_N = \sigma_T = 0.8$, $V_R = 0.05$.

Given $\mathbf{a}_{aero,V}$, the expression of the aerodynamic acceleration in the O_I frame becomes:

$$\mathbf{a}_{aero} = R_{V \rightarrow I} \cdot \mathbf{a}_{aero,V} \quad (15)$$

where $R_{V \rightarrow I}$ is the rotation matrix to transform vectors from the O_V frame to the O_I frame, which depends on the sailcraft position and velocity.

2.2.2.1 Atmospheric Density Model

The atmospheric density ρ used in Eq. (12) is found through an averaging technique based on the NRLMSISE-00* model available in Matlab® [19]. This density averaging process is adopted to decrease the simulation runtime at the cost of slightly reducing the accuracy of the results. The routine is as follows:

- Given the initial sailcraft state, $\mathbf{X}_0 = \mathbf{X}(t_0)$, its osculating Keplerian orbit is found.
- A time interval $[t_0, t_0 + \Delta t]$ is considered, with $\Delta t = P/\text{SpO}$, where P is the osculating orbit’s period and SpO a user-provided parameter corresponding to the number of segments per orbit to consider.

* Throughout this paper, the NRLMISE-00 model is used with the index of the solar radio flux at 10.7 cm and the index of planetary geomagnetic activity taken from the Marshall Space Flight Center’s archived forecast of January 2021, for a percentile value of 50: <https://www.nasa.gov/msfcsolar/archivedforecast> (accessed September 30th, 2021).

- Across the time interval, a set of evenly-spaced time nodes $\{t_0, t_1, \dots, t_{NpS-1} = t_0 + \Delta t\}$ is defined and the corresponding states along the osculating orbit $\{\mathbf{X}_0, \mathbf{X}_1, \dots, \mathbf{X}_{NpS-1}\}$ are found. Note that the number of nodes per orbit segment, NpS, is a user-provided parameter.
- The atmospheric density is computed through the NRLMSISE-00 model for each state of the set $\{\mathbf{X}_0, \mathbf{X}_1, \dots, \mathbf{X}_{NpS-1}\}$, hence resulting in a set of densities $\{\rho_0, \rho_1, \dots, \rho_{NpS-1}\}$ which are averaged to give $\bar{\rho}$.
- The averaged value $\bar{\rho}$ is used as constant atmospheric density to numerically propagate the perturbed dynamics from $\mathbf{X}(t_0)$ to $\mathbf{X}(t_N)$.
- The process is repeated until the end of the simulation, taking t_N and $\mathbf{X}(t_N)$ as t_0 and \mathbf{X}_0 of the next time interval.

2.2.3 J_2 Gravitational Acceleration

The gravitational acceleration due to the Earth's J_2 effect in the O_I frame is given by:

$$\mathbf{a}_{J_2} = -\frac{3R_{\oplus}^2}{2r^5}J_2\mu_{\oplus} \cdot \left[(x_I \hat{\mathbf{x}}_I + y_I \hat{\mathbf{y}}_I) \left(1 - 5\frac{z_I^2}{r^2} \right) + z \left(3 - 5\frac{z_I^2}{r^2} \right) \hat{\mathbf{z}}_I \right] \quad (16)$$

where x_I , y_I , and z_I are the Cartesian coordinates of the sailcraft in the ECI frame and $J_2 = 1.082626925639 \cdot 10^{-3}$ is the Earth's J_2 gravitational field constant of the JGM-2 geopotential model [14].

3. Optimal Control Problem

The optimal control problem considered in the present study builds on the one first investigated by McInnes in [1], where control laws to maximize the instantaneous rate of change of any given orbital element were found under unperturbed, ideal solar-sail dynamics. Hereinafter the same maximization problem will be considered, however also taking into account aerodynamic and gravitational perturbations in the equations of motion and control.

By referring to the generic orbital element as \mathfrak{c} , the optimization problem at hand can be defined as finding the optimal control vector $\mathbf{u}(t) = \hat{\mathbf{n}}(t)$ maximizing the cost function $J(\mathbf{u}(t)) = \mathfrak{c}(\mathbf{u}(t))$ at any given time, subject to the dynamics described in Section 2. When the rate of change of a given orbital element is expressed through a Lagrange planetary equation, the cost function assumes the following form [1]:

$$J(\mathbf{u}(t)) = \mathfrak{c}(\mathbf{u}(t)) = \mathbf{a}(\mathbf{u}(t)) \cdot \boldsymbol{\lambda} \quad (17)$$

where \mathbf{a} is the sum of the accelerations on the right-hand side of Eq. (7) and $\boldsymbol{\lambda}$ is the so-called primer vector, which points along the optimal thrusting direction $\hat{\boldsymbol{\lambda}}$ that

maximizes the orbital element's rate of change. It is worth noting that although the J_2 acceleration, \mathbf{a}_{J_2} , influences the orbital element rate of change (and therefore the cost function $J(\mathbf{u})$), it does not explicitly depend on the control vector \mathbf{u} , as shown in Eq. (7). Consequently, the problem of maximizing $J(\mathbf{u})$ at any time is independent of the J_2 acceleration. For this reason, hereinafter only the SRP and aerodynamic accelerations are considered in the control optimization process, whereas the J_2 acceleration is taken into account only in the propagation of the EoM.

To solve this optimization problem, three different approaches are employed in this paper: an SRP-based optimization, an aerodynamic-based optimization, and a full-dynamics optimization. These optimization techniques are discussed in the following sections and can be applied to find the optimal sail orientation at a specific instant in time. However, during the sailcraft trajectory propagation such algorithms can be applied at each integration time step, hence yielding a sequence (history) of optimal sail normal directions representing the optimal steering law sought.

3.1 Solar Radiation Pressure-based Optimization

The SRP-based optimization method is employed when the SRP acceleration is the predominant acceleration (e.g., for high-altitude orbits). In this case, the aerodynamic acceleration is considered in the propagation of the EoM but neglected in the optimization process, therefore largely simplifying the optimal control computation. Under this assumption, the optimal control history $\mathbf{u}^*(t)$ is found using the method devised by McInnes in [1], where an analytical formulation to compute locally optimal steering laws is presented. This method is based on the idea of considering all the achievable SRP accelerations – which form a so-called acceleration envelope (AE) surface – and finding the optimal sail attitude corresponding to the acceleration vector with the largest component in the direction $\hat{\boldsymbol{\lambda}}$. Because of the simple expression of the SRP acceleration in the sunlight frame (see Eq. (8)), the optimal cone and clock angles of the sail normal, α^* and δ^* , can be computed analytically at each moment in time and, from these, the corresponding optimal control history, $\mathbf{u}^*(t) = \hat{\mathbf{n}}_I^*(t)$, can be found.

3.2 Aerodynamic-based Optimization

The aerodynamic-based optimization method is employed when the aerodynamic acceleration is the predominant acceleration (e.g., for low-altitude orbits or when in eclipse). In this case, the SRP acceleration is considered in the propagation of the EoM but neglected in the optimization process. Similar to the method described in Section 3.1, the optimal sail attitude is found by imposing that the aerodynamic acceleration component along $\hat{\boldsymbol{\lambda}}$ is maximized. However, because of

the complex expression of the aerodynamic AE surface, the sail optimal attitude angles are found using a root-finding method. Since the aerodynamic AE surface is symmetric with respect to the \hat{x}_V -axis direction, hereinafter the section of this surface with a plane passing through the \hat{x}_V -axis will be considered, which corresponds to an AE curve. An illustration of this curve in the (\hat{L}, \hat{D}) plane is given in Fig. 4, where the variables used to describe the optimization procedure are also shown. By using Eq. (12), the angle ψ measured from the direction \hat{D} to the acceleration vector \mathbf{a}_{aero} can be defined as:

$$\psi = \tan^{-1}(\|\mathbf{L}\|/\|\mathbf{D}\|) = \tan^{-1}(C_L/C_D) \quad (18)$$

As shown by Eq. (13) and (14), C_L and C_D are functions of ζ , and therefore so is ψ . Its maximum value, ψ_{max} , can then be found by imposing:

$$\frac{d\psi}{d\zeta} = 0 \Leftrightarrow \frac{d}{d\zeta} \left(\frac{C_L}{C_D} \right) = \frac{C'_L C_D - C_L C'_D}{C_D^2} = 0 \quad (19)$$

In Eq. (19), C'_D and C'_L are the derivatives of C_D and C_L with respect to ζ :

$$C'_D = -2\sigma_T \sin \zeta - [2\sigma_N V_R + 3(2 - \sigma_N - \sigma_T) \cos \zeta] \sin 2\zeta \quad (20)$$

$$C'_L = [(2 - \sigma_N - \sigma_T) \cos \zeta]/2 + 2\sigma_N V_R \cos 2\zeta + 3[(2 - \sigma_N - \sigma_T) \cos 3\zeta]/2 \quad (21)$$

Equation (19) was solved using Matlab[®]'s root-finding function *fzero* with a tolerance of 10^{-10} rad. The angle $\psi_\lambda \in [0, \pi]$ is measured from the direction \hat{D} to the direction $\hat{\lambda}$ and based on its value two different scenarios can be defined. If $\psi_{max} < \psi_\lambda - \pi/2$, the aerodynamic acceleration vector with the largest component along $\hat{\lambda}$ is a zero vector, i.e., the sail is oriented parallel to the wind flow with an optimal attitude angle of $\zeta^* = \pi/2$. Instead,

if $\psi_{max} \geq \psi_\lambda - \pi/2$, a non-trivial solution for ζ^* exists, which can be found by imposing that the direction perpendicular to $\hat{\lambda}$ and the tangent to the AE curve, $\hat{\tau}$, are aligned, see Fig. 4. This condition is equivalent to:

$$\varepsilon - (\psi_\lambda - \pi/2) = 0 \quad (22)$$

where $\varepsilon \in [-\pi/2, \pi/2]$ is a function of ζ and is defined as the angle measured from the direction \hat{D} to the direction $\hat{\tau}$:

$$\varepsilon = \tan^{-1}(C'_L/C'_D) \quad (23)$$

Note that ε is illustrated in Fig. 4 with the subscript “(-)” to indicate the direction in which this angle decreases. The non-trivial solution ζ^* can be found by solving Eq. (22) with a root-finding method (again, in the present work, Matlab[®]'s *fzero* function was used with a tolerance of 10^{-10} rad). After computing the angle ζ^* , the optimal direction of the normal vector in the ECI frame, \hat{n}_I^* , can be found by considering the aerodynamic symmetry of the problem, for which \hat{n} always lies in the (\hat{L}, \hat{D}) plane and is coplanar with \hat{v} and $\hat{\lambda}$. Given the latter two directions expressed in the ECI frame, \hat{v}_I and $\hat{\lambda}_I$, it is possible to compute the optimal direction \hat{n}_I^* in the (\hat{L}, \hat{D}) plane at an angular distance ζ^* from \hat{v}_I as:

$$\hat{n}_I^* = \cos(-\zeta^*) \hat{v}_I + \sin(-\zeta^*) \left[\frac{\hat{v}_I \times \hat{p}}{\|\hat{v}_I \times \hat{p}\|} \times \hat{v}_I \right] \quad (24)$$

where $\hat{p} = \hat{\lambda}_I$ if $\zeta^* \neq \pi/2$. If $\zeta^* = \pi/2$, no lift or drag is generated by the sail and any direction of \hat{n} perpendicular to \hat{v} is optimal. Here, the optimal sail normal direction, \hat{n}_I^* , is arbitrarily chosen to be the direction with the smallest possible angle with the sailcraft inertial position unit vector, \hat{r} , such that $\hat{p} = \hat{r}$ in Eq. (24).

The sail normal direction found through Eq. (24) does not take into account the direction of sunlight, \hat{s} . As such,

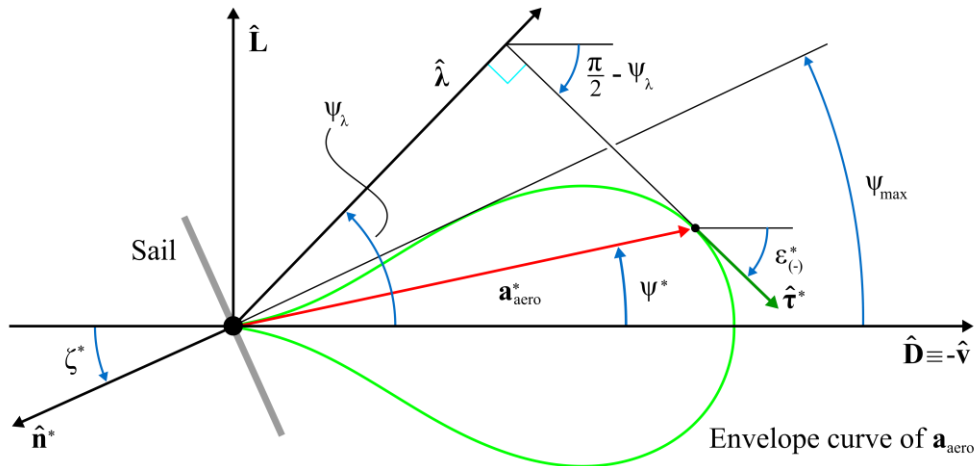


Fig. 4. Envelope curve of aerodynamic acceleration in the (\hat{L}, \hat{D}) plane and variables used to find the optimal aerodynamic acceleration.

it is possible that $\hat{\mathbf{n}}_i^*$ has a component in the direction of the Sun, meaning that the cone angle α is not defined and the SRP acceleration cannot be computed (see Sections 2.1.2 and 2.2.1). This issue can be solved by considering the aerodynamic symmetry of the sail, for which the same aerodynamic acceleration is found for both $\hat{\mathbf{n}}_i^*$ and $-\hat{\mathbf{n}}_i^*$. Based on this, a final check on the direction $\hat{\mathbf{n}}_i^*$ can be implemented. If $\hat{\mathbf{n}}_i^* \cdot \hat{\mathbf{s}} \geq 0$, $\hat{\mathbf{n}}_i^*$ has no component in the direction of the Sun and therefore it can be taken as the final optimal sail normal direction. Conversely, if $\hat{\mathbf{n}}_i^* \cdot \hat{\mathbf{s}} < 0$, $\hat{\mathbf{n}}_i^*$ is switched in sign and $-\hat{\mathbf{n}}_i^*$ is taken as the optimal sail normal vector.

3.3 Full-Dynamics Optimization

The full-dynamics optimization technique is used when the aerodynamic and SRP accelerations are of comparable magnitudes. Similar to the procedures used in Sections 3.1 and 3.2, an AE surface is defined and the sail orientation maximizing the acceleration component along $\hat{\lambda}$ is sought. However, when considering both SRP and aerodynamics the set of all possible sail accelerations forms a highly-nonlinear envelope surface whose shape is time variant. Indeed, while the SRP-based and aerodynamic-based AE surfaces presented in Sections 3.1 and 3.2 are shape-invariant when expressed in the sunlight and velocity reference frames, respectively, the shape of the full-dynamics AE surface depends on the relative orientation of the instantaneous $\hat{\mathbf{s}}$ and $\hat{\mathbf{v}}$ directions, as well as the relative magnitude of the SRP characteristic acceleration, a_c , compared to the maximum aerodynamic acceleration, $a_{aero,max}$. In addition, the envelope surface can also be self-intersecting, meaning that different sail attitudes can result in the same total acceleration vector. An example of such a surface is given for $\hat{\mathbf{s}} \perp \hat{\mathbf{v}}$ and $a_c = a_{aero,max}$ in Fig. 5, where the corresponding SRP and aerodynamic AE surfaces are also shown for comparison. Because of

the complex, time-variant shape of the AE surface and to the best of the authors' knowledge, no analytical solution to the optimization problem exists and therefore a numerical approach was employed instead. The basic idea behind the proposed approach is to first find the global optimal solution of the cost function $J(\mathbf{u})$ for a large variety of scenarios and subsequently interpolate these pre-computed optimal solutions at each time step in the trajectory propagation to retrieve an interpolated global optimum. In this way, the attitude optimization computation is completely separated from the trajectory propagation, thereby allowing the latter to be performed with low computational effort. Hereinafter this optimization method is referred to as the "Pre-run Optimization and in-run INTERpolation" (POINT) method. The two phases of the method, the optimization and interpolation phases, are described in detail in Sections 3.3.1 and 3.3.2.

3.3.1 Pre-run Optimization Phase

The pre-run optimization phase of the POINT method aims to solve the optimization problem for a large set of different scenarios, i.e., for a large variety of combinations of AE shapes and $\hat{\lambda}$ directions. To do so, the optimization problem is parametrized by four parameters: R , η , θ , and ϕ .

- The coefficient R represents the ratio of the maximum SRP acceleration to the maximum aerodynamic acceleration and its value affects the AE shape. This coefficient indicates to what extent the AE shape is similar to the AE shape of the pure SRP acceleration or pure aerodynamic acceleration. For example, for increasing values of R , the SRP acceleration increasingly dominates the aerodynamic acceleration, meaning that the AE shape becomes more similar to the SRP one. On the other hand, for R values close to zero, the aerodynamic acceleration is dominant so that the AE shape tends to resemble

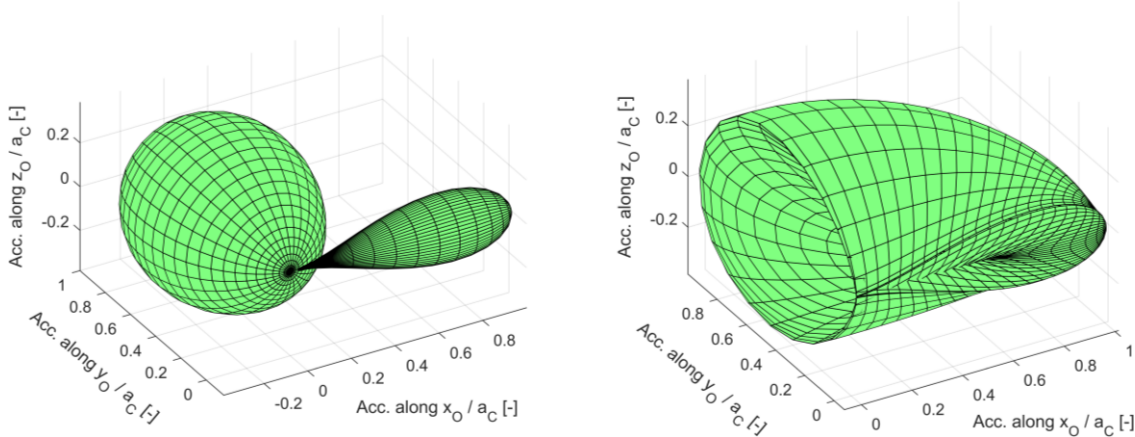


Fig. 5. SRP and aerodynamic AE surfaces (left) and full dynamics AE surface (right) in the O_0 frame, for $\hat{\mathbf{s}} = \hat{\mathbf{y}}_0$ and $a_c = a_{aero,max}$.

the AE shape of the pure aerodynamic case. By taking into account that the maximum SRP acceleration is equal to the solar-sail characteristic acceleration and that the maximum aerodynamic acceleration is achieved for $\zeta = 0$ (i.e., when the sail is perpendicular to the wind flow), R can be expressed using Eq. (9), (12), (13), and (14) as:

$$R = \frac{a_c}{a_{aero,max}} = \frac{S_{\oplus}}{c} \frac{2}{\rho v^2} \frac{1}{[2 - \sigma_N(1 - V_R)]} \quad (25)$$

Since both the SRP and aerodynamic accelerations are inversely proportional to the sail loading parameter σ , R is independent of σ . This result implies that the AE shape – and thus the entire optimization process – is independent of the sail loading parameter.

- The parameter η determines the relative orientation of the SRP and aerodynamic AE surfaces and its definition is given in Section 2.1.4. Together with R , it uniquely defines the AE shape of the full-dynamics case, which results from combining the two separate (i.e., pure SRP and pure aerodynamic) AE surfaces. An example is given in Fig. 5, where the combination of the AE surfaces in the left plot generates the one in the right plot.
- The angles θ and ϕ represent the spherical coordinates of the $\hat{\lambda}$ direction in the O_0 frame (see Fig. 3).

Each set $\{R, \eta, \theta, \phi\}$ represents a specific optimization problem which can be solved numerically to find the corresponding optimal sail attitude. To achieve this, in this paper a grid search is performed over the angles ζ and γ of the sail normal direction in the optimization frame. To explore the entire parameter space, a four-dimensional grid of discrete values for R, η, θ , and ϕ is created across the following domains: $R \in [R_{min}, R_{max}]$, $\eta \in [0, \pi]$, $\theta \in [0, 2\pi]$, and $\phi \in [0, \pi/2]$. R_{min} and R_{max} are two threshold parameters determining when the full dynamics optimization should be used instead of the aerodynamic-based optimization ($R > R_{min}$) or the SRP-based optimization ($R < R_{max}$). Their values have been determined based on thorough testing and are specified in Section 4. Finally, it is worth noting that only positive values of ϕ are considered because of the symmetry of the AE surface with respect to the (\hat{x}_0, \hat{y}_0) plane. Due to this symmetry, each pair of angles $\pm\phi$ corresponds to optimal normal directions in the O_0 frame, \hat{n}_0^* , that differ only in the sign of the component along the \hat{z}_0 direction, i.e., $\hat{n}_0^* = [n_{0,x}^*, n_{0,y}^*, \pm n_{0,z}^*]^T$. Therefore, whenever a $\hat{\lambda}$ direction with $\phi < 0$ is encountered during the trajectory propagation, the optimal normal direction \hat{n}_0^* computed for $-\phi$ (> 0) in the pre-run optimization phase is

retrieved and the sign of its $n_{0,z}^*$ -component is changed to obtain the optimal attitude for $\phi < 0$.

3.3.2 In-run Interpolation Phase

To describe the interpolation process adopted in the POINT method, each set of variables $\{R, \eta, \theta, \phi\}$ will be represented as a point $\mathcal{S} = [S_1, S_2, S_3, S_4]^T = [R, \eta, \theta, \phi]^T$ in a four-dimensional vector space. In this way, each grid point computed in the pre-run optimization phase is represented by $\mathcal{S} \in \mathbb{R}^{4 \times 1}$, while the set of all grid points is $\Sigma = \{\mathcal{S}_1, \mathcal{S}_2, \dots, \mathcal{S}_N\} \in \mathbb{R}^{4 \times N}$, with N equal to the total number of grid points.

At each time step of the trajectory propagation, specific values for R, η, θ , and ϕ are encountered which identify a target point $\mathcal{S}_t = [S_{t,1}, S_{t,2}, S_{t,3}, S_{t,4}]^T$. In general, \mathcal{S}_t will be different from any of the points \mathcal{S} available in Σ . However, it is always possible to find a subset of points $\Sigma_{NBH} \subset \Sigma$ close to \mathcal{S}_t that enclose the region of space where \mathcal{S}_t is located. This region is obtained by considering, for each component $S_{t,k}$, the two closest neighboring values in the pre-optimized grid, $S_{t,k}^-$ and $S_{t,k}^+$, such that $S_{t,k} \in [S_{t,k}^-, S_{t,k}^+]$, with $k = 1, \dots, 4$. This results in $2^4 = 16$ possible combinations representing the coordinates of the points in $\Sigma_{NBH} \in \mathbb{R}^{4 \times 16}$:

$$\Sigma_{NBH} = \left\{ \begin{array}{l} \mathcal{S}_{NBH,1} = [S_{t,1}^-, S_{t,2}^-, S_{t,3}^-, S_{t,4}^-]^T \\ \mathcal{S}_{NBH,2} = [S_{t,1}^-, S_{t,2}^-, S_{t,3}^-, S_{t,4}^+]^T \\ \mathcal{S}_{NBH,3} = [S_{t,1}^-, S_{t,2}^-, S_{t,3}^+, S_{t,4}^-]^T \\ \mathcal{S}_{NBH,4} = [S_{t,1}^-, S_{t,2}^-, S_{t,3}^+, S_{t,4}^+]^T \\ \mathcal{S}_{NBH,5} = [S_{t,1}^-, S_{t,2}^+, S_{t,3}^-, S_{t,4}^-]^T \\ \vdots \\ \mathcal{S}_{NBH,16} = [S_{t,1}^+, S_{t,2}^+, S_{t,3}^+, S_{t,4}^+]^T \end{array} \right\} \quad (26)$$

Since each point in Σ_{NBH} corresponds to an optimal sail orientation computed in the pre-run optimization phase, a set $\Gamma_{NBH} \in \mathbb{R}^{3 \times 16}$ of 16 optimal normal directions in frame O_0 , \hat{n}_0^* , is also given. The interpolation of these normal directions is performed through a normalized inverse distance weighted (IDW) technique [20] and applied to the problem at hand as follows. Before the interpolation is performed, \mathcal{S}_t and the points in Σ_{NBH} are normalized [†] to restrict the domain of their four components to $[0, 1]$, thus resulting in the normalized target point $\bar{\mathcal{S}}_t$ and neighboring set $\bar{\Sigma}_{NBH} = \{\bar{\mathcal{S}}_{NBH,1}, \dots, \bar{\mathcal{S}}_{NBH,16}\}$. From these, the vector $\mathbf{q} = [q_1, \dots, q_{16}]^T$ is computed which contains the inverses of the Euclidean distances between $\bar{\mathcal{S}}_t$ and $\bar{\mathcal{S}}_{NBH,1}, \dots, \bar{\mathcal{S}}_{NBH,16}$. The inverse distance weight vector, \mathbf{w} , is also calculated as:

[†] In the normalization the Cartesian components of $\hat{\lambda}$ are considered instead of θ and ϕ to avoid discontinuities in the interpolation.

$$\mathbf{w} = [w_1, \dots, w_{16}]^T = (\mathbf{q} \circ \mathbf{q}) / (\mathbf{q}^T \cdot \mathbf{q}) \quad (27)$$

where \circ indicates the element-wise Hadamard product of two vectors [21]. Finally, the optimal normal directions in Γ_{NBH} , i.e., $\hat{\mathbf{n}}_{O,NBH,1}^*, \dots, \hat{\mathbf{n}}_{O,NBH,16}^*$, are used to define the following matrix \mathcal{N} :

$$\mathcal{N} = \begin{bmatrix} \hat{\mathbf{n}}_{O,NBH,1}^* & T \\ \vdots & \\ \hat{\mathbf{n}}_{O,NBH,16}^* & T \end{bmatrix} \quad (28)$$

which is then used to find the final interpolated normal direction, $\hat{\mathbf{n}}_O^*$, as:

$$\hat{\mathbf{n}}_O^* = (\mathcal{N} \cdot \mathbf{w}) / \|\mathcal{N} \cdot \mathbf{w}\| \quad (29)$$

3.3.2.1 Handling of Local Optima

As the neighboring points $\mathbf{S}_{NBH,1}, \dots, \mathbf{S}_{NBH,16}$ consider different values for R , η , θ , and ϕ , they represent optimization problems with slightly different AE shapes and $\hat{\lambda}$ directions. However, due to the high nonlinearity of the problem, in certain cases these different AE shapes and primer vector's directions make the optimal normal directions $\hat{\mathbf{n}}_{O,NBH,1}^*, \dots, \hat{\mathbf{n}}_{O,NBH,16}^*$ differ substantially. Such scenarios take place when the target point considered, \mathbf{S}_t , corresponds to an optimization problem with optimal regions of similar degrees of optimality. In these cases, the cost function values associated to these regions slightly change when moving between neighboring points of \mathbf{S}_t , hence making the global optimum shift from one optimal region to another depending on the specific neighboring point considered. As a consequence, using IDW interpolation on the normal directions $\hat{\mathbf{n}}_{O,NBH,1}^*, \dots, \hat{\mathbf{n}}_{O,NBH,16}^*$ can result in an interpolated solution $\hat{\mathbf{n}}_O^*$ that is far from the true optimum.

To avoid this issue, the POINT method makes use of an algorithm that aims to identify such optimal regions before the interpolation. In this way, it is possible to consider each optimal region separately in the interpolation phase and compute different optimal solutions $\hat{\mathbf{n}}_O^*$, which contain the global optimum. The algorithm is based on the idea that different optimal regions of the solution space correspond to optimal sail normal vectors pointing in different directions. In light of this, it is possible to identify the number of local optima of the optimization problem represented by \mathbf{S}_t by analyzing the angular distances between the optimal normal directions of Γ_{NBH} . This way, different subsets of Γ_{NBH} can be defined that correspond to different clusters of normal directions, which in turn identify the local optimal regions. In this paper the cluster detection has been performed by means of a hierarchical clustering algorithm with single-linkage criterion [22]. The

algorithm computes the norm of the difference of each pair of normal directions in Γ_{NBH} , compares these norms with a threshold value, and, based on it, determines the number of clusters in Γ_{NBH} . More specifically, in this paper the Matlab[®]'s function *cluster* was employed using a distance-based criterion and a hierarchical cluster tree (defined through the function *linkage*) built with a "shortest Euclidean distance" method. The value used for the threshold was $2 \sin(\pi/60)$, corresponding to a minimum angle of 6 deg between normal directions of different clusters. This value was tuned based on the knowledge of the optimization problem under investigation, the number of grid points in Σ , and some trial and error. When the optimization problem is not characterized by multiple optimal regions, the algorithm returns one unique cluster that coincides with Γ_{NBH} and therefore the interpolation routine can be performed as explained in the previous section. Conversely, if different clusters are found, for each cluster in Γ_{NBH} the corresponding points in Σ_{NBH} are taken and the normalization and interpolation routines are performed separately on each subset of Σ_{NBH} to find multiple optimal solutions $\hat{\mathbf{n}}_O^*$. From these, the optimal normal direction corresponding to the largest cost function value is taken as the global optimal solution.

4. Validation

In this section, two cases are discussed which aim to validate the POINT optimization method and show its accuracy, both for an orbit raising steering law and an inclination increase steering law. This is achieved by propagating one single orbit, optimizing its control with the POINT method, and comparing the control profile achieved with a reference solution. In both cases the ACS3 mission scenario is considered, which corresponds to a solar-sail characteristic acceleration of $a_C = 0.05 \text{ mm/s}^2$, a simulation start time of July 1st, 2022 (i.e., the expected deployment date of the solar sail), and the following initial Keplerian elements: semi-major axis (SMA) $a_0 = 7093.1363 \text{ km}$, eccentricity $e_0 = 0$, inclination $i_0 = 98.2489 \text{ deg}$, right ascension of the ascending node $\Omega_0 = 10.5029 \text{ deg}$, argument of perigee $\omega_0 = 0 \text{ deg}$, and true anomaly $\vartheta_0 = 0 \text{ deg}^\ddagger$. Note that these Keplerian elements identify a circular, Sun-synchronous orbit with altitude $h_0 = 715 \text{ km}$ and local time of the ascending node (LTAN) at 6AM (dawn-dusk orbit). The analyses discussed in this section will not consider the J_2 gravitational acceleration in the EoM. This choice is justified by the fact that the J_2 acceleration has no secular effect on the target orbital elements analyzed (i.e., the SMA and inclination), but only a short-term periodic effect. Therefore, including the J_2 acceleration would have added significant noise in the results. The atmospheric density is found through the

[‡] ACS3 mission data taken from personal communication with W. Keats Wilkie, NASA Langley Research Center, September 2021.

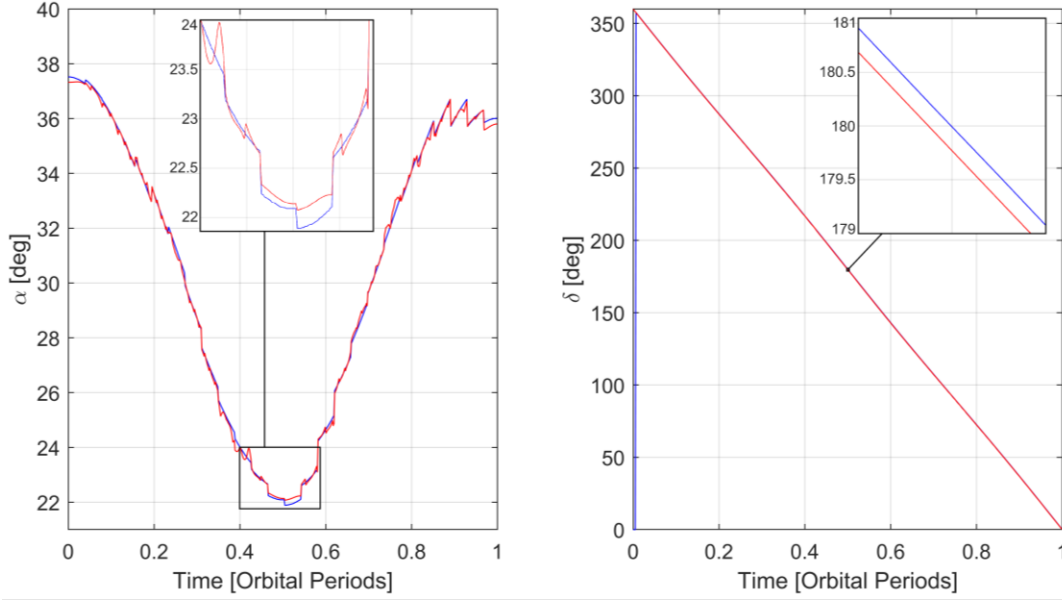


Fig. 6. Orbit raising: control profile of the reference solution (blue) and POINT solution (red) over one orbital period.

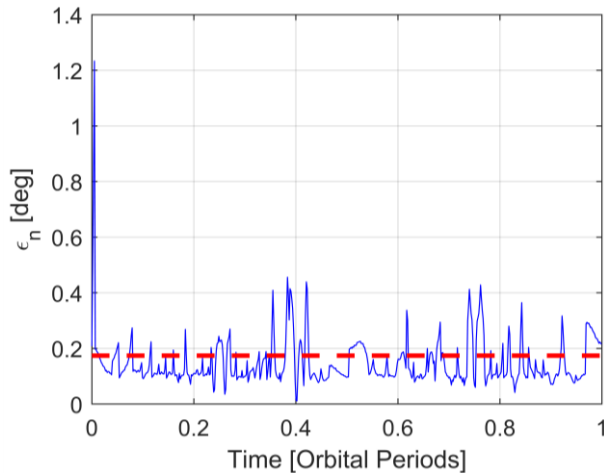


Fig. 7. Orbit raising: angular error between the sail normal directions found by the POINT method and grid search (blue) and RMS of the angular error over one orbital period (red, dashed).

averaged NRLMSISE-00 model with $Sp0 = 25$ and $NpS = 4$. Propagations of one orbital period using MATLAB[®]'s *ode45* integrator are performed, with absolute and relative tolerances of 10^{-8} . The reference solutions for both steering laws are found by performing a grid search at each propagation time step, with steps of 0.01 deg for the angles α and δ . The POINT optimization method uses an optimized grid Σ where the components R , η , θ , and ϕ of the points $S \in \Sigma$ are spaced with steps equal to $\Delta R = 1.21$ and $\Delta\eta = \Delta\theta = \Delta\phi = 1$ deg. It should be noted that while $\Delta\eta$, $\Delta\theta$, and $\Delta\phi$ represent the differences between adjacent angular values of the grid, ΔR represents the *ratio* of consecutive R values. This means that given a value R_k of the grid,

the adjacent one, R_{k+1} , is found as $R_{k+1} = R_k \cdot \Delta R$. The acceleration ratio domains considered are $R \in [1/4, 50]$ and $R \in [1/100, 30]$ for the orbit raising and inclination increase steering laws, respectively. Finally, the grid search of the pre-run optimization phase of POINT was performed using $\Delta\gamma = \Delta\zeta = 0.1$ deg as angular steps.

4.1 Orbit Raising

For the orbit raising steering law, the control profiles of the reference solution and the POINT solution are given in Fig. 6. As can be appreciated from the zoomed plots of the cone and clock angle profiles, the POINT solution (in red) accurately approximates the reference solution (in blue). Also, from Fig. 6 it can be noted that instantaneous jumps in cone angle take place, both in the reference and POINT solutions. This is due to the averaging procedure of the atmospheric density model, which yields a step-wise variation in the density along the orbit and, therefore, also in the acceleration ratio. This in turn affects the control computation procedure, leading to the sudden variations in α shown in the figure. As a measure of the error in optimal sail normal direction as computed by the POINT method, the angular displacement, ϵ_n , between the sail normal direction of the POINT method and the reference solution is computed at each time step. The result is displayed in Fig. 7, where the dashed line indicates the root mean square (RMS) of ϵ_n , equal to 0.1742 deg. It should be noted that the RMS of ϵ_n depends on the angular steps $\Delta\eta$, $\Delta\theta$, $\Delta\phi$, $\Delta\gamma$, and $\Delta\zeta$ used in the pre-run optimization phase of POINT and are of comparable magnitudes, as one would

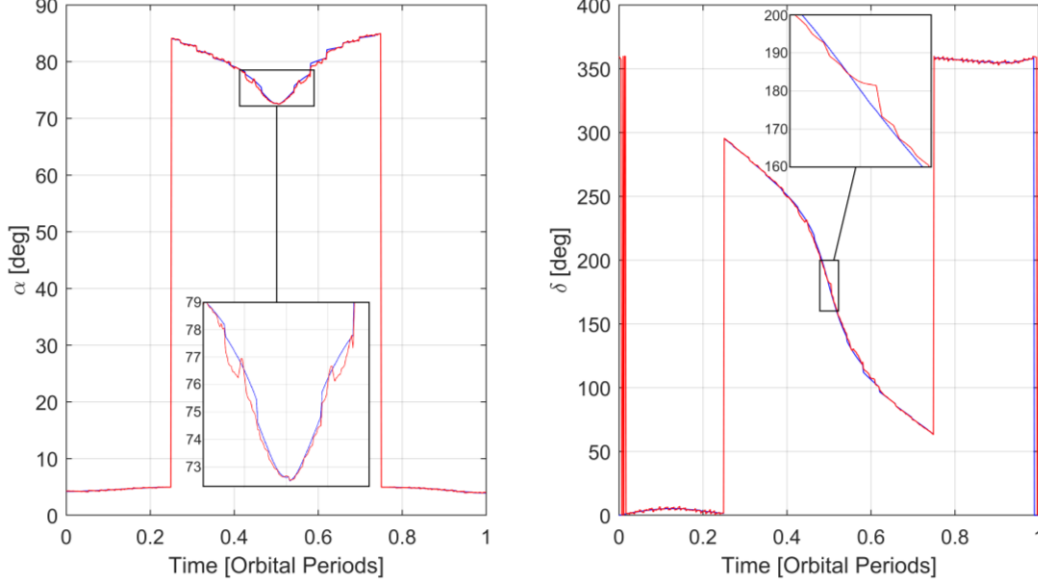


Fig. 8. Inclination increase: control profile of the reference solution (blue) and POINT solution (red) over one orbital period.

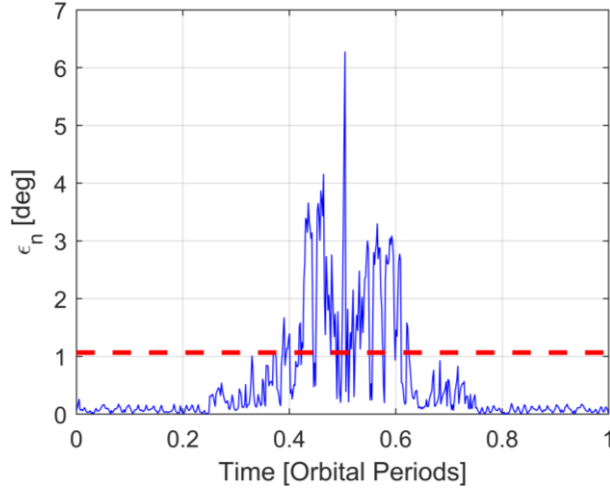


Fig. 9. Inclination increase: angular error between the sail normal directions found by the POINT method and grid search (blue) and RMS of the angular error over one orbital period (red, dashed).

expect when performing an interpolation. To have a measure of the POINT method's accuracy, the relative error of the SMA increase, $\epsilon_{\Delta a,rel}$, can be considered. This is defined as:

$$\epsilon_{\Delta a,rel} = |(\Delta a - \Delta a_{ref})/\Delta a_{ref}| \quad (30)$$

where Δa and Δa_{ref} are the increases in SMA of the POINT and reference solutions, respectively. Its value after one orbital period is of $\epsilon_{\Delta a,rel} = 2.7537 \cdot 10^{-5}$.

4.2 Inclination Increase

The α and δ angle profiles for the inclination steering laws found by the POINT method and grid search are

given in Fig. 8. Here, it can be noted that the POINT solution closely resembles the reference solution. Nonetheless, the POINT solution manages to approximate the reference solution better during the first and last quarter of the orbit than in the middle part of the orbital revolution. This becomes even clearer in the zoomed plots of Fig. 8, as well as in Fig. 9, which displays the evolution of ϵ_n . In particular, the latter figure shows that the POINT method experiences difficulties in finding the true optimal solution, leading to displacements in the sail normal direction in the order of some degrees. The displacements observed are due to the intrinsic difficulty in increasing the inclination in this middle part of the orbit. Indeed, within this segment of the orbit, every non-zero, out-of-plane acceleration achievable by the sail points in the opposite direction of $\hat{\lambda}$ and would therefore yield a negative Δi . Consequently, the optimal attitude is the one that minimizes the out-of-plane acceleration to induce no change in inclination. However, multiple different sail attitudes lead to a Δi close to zero, hence making the search for the global optimal attitude hard for the POINT method. The relative error of the inclination increase, $\epsilon_{\Delta i,rel}$, is defined similar to $\epsilon_{\Delta a,rel}$ as:

$$\epsilon_{\Delta i,rel} = |(\Delta i - \Delta i_{ref})/\Delta i_{ref}| \quad (31)$$

where Δi_{ref} and Δi are the increases in inclination achieved by the reference optimal solution and by the POINT solution, respectively. Despite the displacements in the sail normal direction in the middle part of the orbit, the relative error achieved at the end of the propagation is $\epsilon_{\Delta i,rel} = 8.4872 \cdot 10^{-6}$, which is deemed acceptable.

5. Results and Analysis

In this section, the POINT method will be used to compute the control laws to maximize the semi-major axis or inclination change, starting from different Earth-centered orbits. For each of these target orbital elements, a parametric analysis will be performed to determine the achievable increase in the orbital element starting from different initial orbits, for different solar-sail characteristic accelerations, and different solar activity. In this way, a wide variety of scenarios is considered and a thorough analysis of the orbit change capabilities of solar sailing for Earth-bound missions is achieved. The characteristic accelerations to be considered vary between 10^{-2} and 10^{-1} mm/s² to represent the current and near-future solar-sail technology. For example, the first solar sail launched into orbit, IKAROS, had a characteristic acceleration of $5.8 \cdot 10^{-3}$ mm/s², while NASA's upcoming ACS3 and NEA Scout missions will achieve solar-sail characteristic accelerations of $5.0 \cdot 10^{-2}$ and $6.3 \cdot 10^{-2}$ mm/s², respectively [23]. To consider a broad range of initial conditions representative of orbits commonly used for scientific LEO missions, the analyses are performed for circular, Sun-synchronous orbits with an LTAN at 6 AM (dawn/dusk) or 12 AM (noon/midnight) and altitudes ranging between 300 km and 1000 km. Finally, to account for the effect of solar activity on the atmospheric density, two different starting dates are considered: September 23, 2023 and September 23, 2030, corresponding to maximum and minimum solar activity, respectively. It should be noted that these dates are chosen arbitrarily within longer-duration periods of solar maximum and minimum activity, and correspond to the autumn equinoxes, for which the Sun "orbits" in the Earth's equatorial plane. Other dates within the periods of solar maximum/minimum can of course be considered, which would then correspond to slightly different orientations of the science orbit with respect to the Sun and which, therefore, would lead to slightly different results of the analyses. The EoM include the SRP, aerodynamic, and J_2 accelerations and take into account eclipses. For each scenario, an orbit propagation of 10 days is performed using Matlab[®]'s *ode45* integrator, with absolute and relative tolerances of 10^{-12} . The averaged NRLMSISE-00 atmospheric density model is used with $SpO = 25$ and $NpS = 4$. Finally, the POINT optimization method is used with the same optimized grid Σ presented in Section 4.

5.1 Orbit Raising

The results of the parametric analysis performed for the orbit raising steering law appear in Fig. 10. The four plots display the increase in SMA, Δa , achieved after 10 days for different combinations of LTAN and solar activity. Each plot shows 10 curves for 10 different values of the characteristic acceleration. The figure

shows that, for a given LTAN, the solar activity determines the minimum altitude for which orbit raising is still possible. Conversely, the effect of a different solar activity on Δa becomes negligible at high altitudes; the curves asymptotically tend to the same values. This is because the air density decreases exponentially with orbital altitude, reaching a point at which the aerodynamic drag becomes negligible and similar SMA increases are found even for largely different solar activities. Comparison of the plots for different LTAN values and the same solar activity shows that the effect of changing the LTAN from 6AM (dawn/dusk) to 12AM (noon/midnight) reduces the SMA increase. This is due to the presence of eclipses for a noon/midnight orbit, during which no SRP acceleration is exerted on the sail (no increase in SMA) and the sail is oriented parallel to the wind flow to minimize drag.

The results in Fig. 10 for $a_c = 5.0 \cdot 10^{-2}$ mm/s² are combined in Fig. 11 to gain further insights in the ranges of achievable SMA increase. For example, if one considers a specific LTAN, the two curves for minimum and maximum solar activity enclose the region of maximum SMA increase for any solar activity. A specific example is given by the two marks that represent the ACS3 mission with a simulation start date of July 1st, 2022. This date corresponds to an intermediate solar activity and, as such, the Δa values achieved for the ACS3 mission lie well within the above-mentioned region. Alternatively, the curves for a fixed solar activity but with different LTANs can be considered. Since LTANs at 6AM and 12AM represent the orbits with the shortest and longest eclipsing time, respectively, any initial orbit with an LTAN different from 6AM or 12AM will show an SMA increase within the region enclosed by these two curves. Fig. 11 shows that the largest SMA increases are achieved at solar minimum and for an LTAN at 6AM, whereas the smallest values for Δa are achieved at solar maximum and for an LTAN at 12AM. These two curves correspond to the overall best and worst orbit scenarios and for any circular, Sun-synchronous orbit the achievable increase in SMA is always enclosed by these curves.

The results in Fig. 10 and Fig. 11 can be used to inform the preliminary design of solar-sail LEO missions. In fact, although the results are given only for a propagation time of 10 days, the achievable SMA increase for longer propagation times can be retrieved from the same results by consulting the plots in an iterative fashion: consider a given initial altitude, h_0 , with an SMA increase Δa_0 , then the same plot can be reused starting from a new altitude $h_1 = h_0 + \Delta a_0$ to retrieve Δa_1 , which in turn is used to define h_2 and so

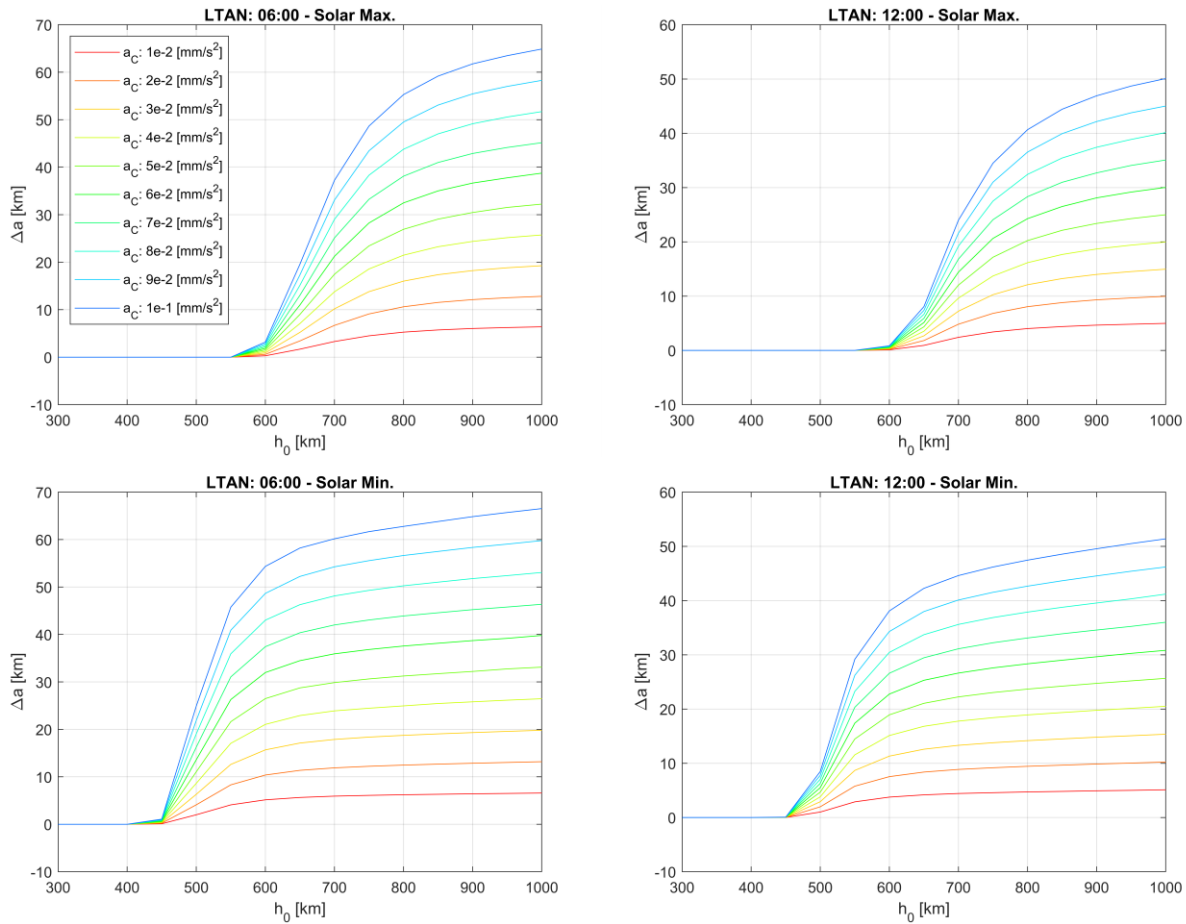


Fig. 10. Orbit raising steering law: SMA increase as a function of the initial altitude for different LTAN values and solar activities.

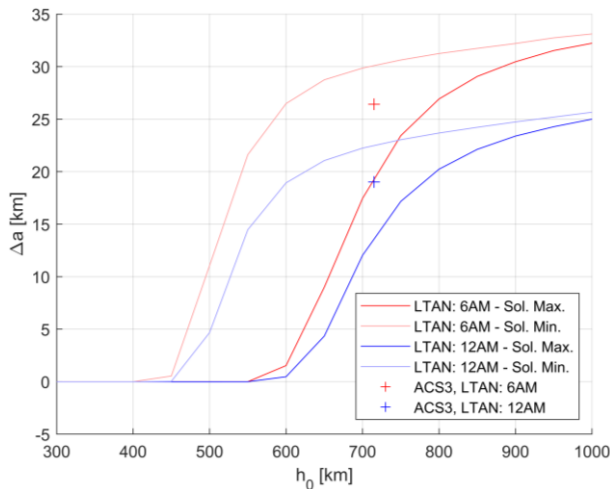


Fig. 11. Orbit raising steering law: SMA increase for the orbit raising steering law with $a_c = 5 \cdot 10^{-2} \text{ mm/s}^2$.

forth. At each iteration of this process the mission duration increases by 10 days, so that the iterations can be stopped until the desired mission duration is obtained.

5.2 Inclination Increase

The results of the parametric analysis for the inclination increase steering law appear in Fig. 12. The truncation of the curves at low altitude is due to a rapid loss in altitude when increasing the inclination under the effects of atmospheric drag. The orbit propagation is stopped when an altitude lower than 100 km is reached within 10 days. As can be seen, the altitude at which this condition occurs depends on the characteristic acceleration, solar activity, and LTAN. An interesting trend which can be appreciated in all four plots of Fig. 12 is the steep gradient in the inclination increase for decreasing altitudes: when lowering the orbital altitude, not only the drag increases, but also the aerodynamic lift, which provides the out-of-plane acceleration used to change the inclination. At higher altitudes, no significant change in the inclination increase as a function of altitude can be observed. Conversely, a strong correlation between the inclination increase and the solar-sail characteristic acceleration can be noted.

Similar to Fig. 11 for the orbit raising case, Fig. 13 displays the variation in inclination increase for a characteristic acceleration of $a_c = 5 \cdot 10^{-2} \text{ mm/s}^2$, for

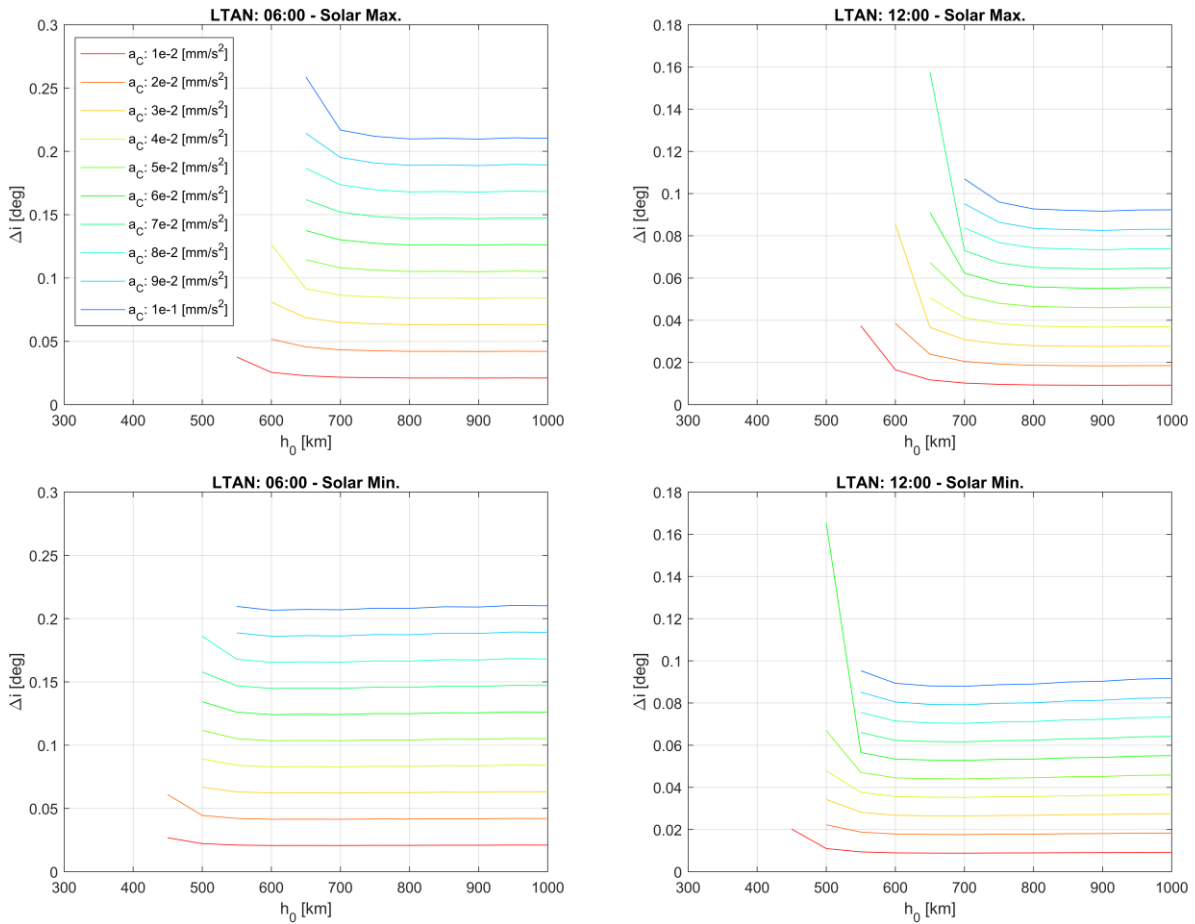


Fig. 12. Inclination increase steering law: inclination increase as a function of the initial altitude for different LTAN values and solar activities.

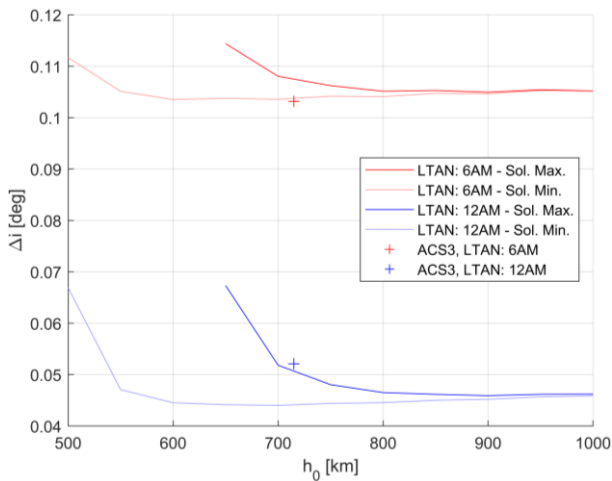


Fig. 13. Inclination increase steering law: inclination increase for the orbit raising steering law with $a_c = 5 \cdot 10^{-2} \text{ mm/s}^2$.

minimum and maximum solar activities and LTANs at 6AM and 12AM. For increasing values of h_0 , the results for the solar minimum case and solar maximum case

converge to the same values. This is because the atmospheric density decreases and the inclination increase is produced solely by the SRP acceleration, which is equal in both cases. Fig. 13 also shows the inclination increases achievable by the ACS3 mission at an intermediate solar activity. As can be seen, the values for Δi fall slightly below or above the regions enclosed by the minimum and maximum solar activity. By further analysing these results, it was found that these differences are due to the different simulation start date of July 1st, 2022 instead of the autumn equinox. This results in a different orientation of the ACS3's initial orbit with respect to the Sun and hence slightly different values for Δi .

6. Conclusions

In this paper a novel method to optimize Earth-bound solar-sail orbits in the presence of atmospheric drag has been presented and employed on a wide variety of scenarios. To reduce the computational effort required, an averaged atmospheric density model has been introduced. The optimal control problem has been analyzed thoroughly for different dynamical regimes,

namely the solar radiation pressure (SRP)-dominated regime, the aerodynamic drag-dominated regime, and the full-dynamics (SRP+drag) regime. To solve the optimization problem in the full-dynamics regime, the POINT optimization method has been introduced, which is based on a pre-run optimization phase and in-run interpolation phase. The pre-run optimization phase takes place before the trajectory propagation and aims to solve the optimal control problem for a broad range of scenarios, in order to store the corresponding optimal sail normal directions. Afterwards, the in-run interpolation of the optimal sail normal directions takes place at each integration time step during the propagation. A validation test has been performed to demonstrate the accuracy and global validity of the optimal solutions found by the POINT method. The method has been applied to an orbit raising steering law and inclination increase steering law on NASA's upcoming ACS3 mission and a range of other circular, Sun-synchronous orbits, differing from each other on the local time of the ascending node, the altitude, and the solar-sail characteristic acceleration considered. The results of the analyses show that the minimum altitude for which orbit raising is achievable varies between 450 and 600 km and strongly depends on the solar activity, while the local time of the ascending node affects the magnitude of the altitude increase. The inclination increase steering law proved to be unsuited for orbits with altitudes below 500 ÷ 650 km, as the sailcraft tends to de-orbit rapidly. Conversely, at high altitudes, increases in inclination are achievable, with their magnitude depending largely on the solar-sail characteristic acceleration.

Acknowledgements

The authors thank W. Keats Wilkie and Sarah M. Cook from NASA Langley Research Center and Andrew Heaton from NASA Marshall Space Flight Center for the numerous, fruitful discussions on the ACS3 mission and all the related information shared.

References

- [1] C. R. McInnes, *Solar Sailing - Technology, Dynamics and Mission Applications*, Springer, 2004.
- [2] M. Macdonald and C. R. McInnes, "Solar Sail Science Mission Applications and Advancement," *Advances in Space Research*, pp. 1702-1716, 2011. DOI: 10.1016/j.asr.2011.03.018.
- [3] B. Dachwald, "Optimal Solar-Sail Trajectories for Missions to the Outer Solar System," *Journal of Guidance, Control, and Dynamics*, vol. 28, no. 6, pp. 1187-1193, 2005. DOI: 10.2514/1.13301.
- [4] M. Macdonald, *Advances in Solar Sailing*, Springer, 2014, pp. 95-113.
- [5] B. Betts, B. Nye, E. Greeson and et al., "LightSail 1 Mission Results and Public Outreach Strategies," in *Proceedings of the 4th International Solar Sailing Symposium*, Kyoto, Japan, 2017.
- [6] D. A. Spencer, B. Betts, J. M. Bellardo, A. Diaz, B. Plante and J. R. Mansell, "The LightSail 2 Solar Sailing Technology Demonstration," *Advances in Space Research*, vol. 67, no. 9, pp. 2878-2889, 2021. DOI: 10.1016/j.asr.2020.06.02.
- [7] W. K. Wilkie, J. M. Fernandez, O. R. Stohlman and et al., "An Overview of the NASA Advanced Composite Solar Sail (ACS3) Technology Demonstration Project," *AIAA Scitech 2021 Forum*, 2021.
- [8] M. Macdonald and C. R. McInnes, "Analytical Control Laws for Planet-Centered Solar Sailing," *Journal of Guidance, Control, and Dynamics*, vol. 28, no. 5, pp. 1038-1048, 2005. DOI: 10.2514/1.11400.
- [9] M. Macdonald and C. R. McInnes, "Realistic Earth Escape Strategies for Solar Sailing," *Journal of Guidance, Control, and Dynamics*, vol. 28, no. 2, pp. 315-323, 2005. DOI: 10.2514/1.5165.
- [10] A. De Iuliis, F. Ciampa, L. Felicetti and M. Ceriotti, "Sailing with Solar and Planetary Radiation Pressure," in *Proceedings of ISSS 2019: 5th International Symposium on Solar Sailing*, Aachen, Germany, 2019. DOI: 10.1016/j.asr.2019.11.036.
- [11] G. Mengali and A. A. Quarta, "Near-Optimal Solar-Sail Orbit-Raising from Low Earth Orbit," *Journal of Spacecraft and Rockets*, vol. 42, no. 5, pp. 954-958, 2005. DOI: 10.2514/1.14184.
- [12] T. O. Morgan, "The Inclination Change for Solar Sails and Low Earth Orbit," *Advances in Astronautical Sciences*, pp. 559-573, 1979.
- [13] V. Stolbunov, M. Ceriotti, C. Colombo and C. R. McInnes, "Optimal Law for Inclination Change in an Atmosphere Through Solar Sailing," *Journal of Guidance, Control, and Dynamics*, vol. 36, no. 5, pp. 1310-1323, 2013. DOI: 10.2514/1.59931.
- [14] J. R. Wertz and W. J. Larson, *Space Mission Analysis and Design*, El Segundo: Microcosm Press and Dordrecht: Kluwer Academic Publishers, 2005.
- [15] C. R. Ortiz Longo and S. L. Rickman, "Method for the Calculation of Spacecraft Umbra and Penumbra Shadow Terminator Points," NASA Center for AeroSpace Information, Linticum Heights, 1995.
- [16] P. Kelly and R. Bevilacqua, "An Optimized Analytical Solution for Geostationary Debris Removal using Solar Sails," *Acta Astronautica*, vol. 162, pp. 72-86, 2019. DOI: 10.1016/j.actaastro.2019.05.055.
- [17] J. A. Storch, "Aerodynamic Disturbances on Spacecraft in Free-Molecular Flow," The Aerospace Corporation, 2002.
- [18] P. C. Hughes, *Spacecraft Attitude Dynamics*, New York: Dover Publications Inc., 2004.
- [19] J. M. Picone, A. E. Hedin and D. P. Drob, "NRLMSISE-00 empirical model of the atmosphere: Statistical comparisons and scientific issues," *Journal of Geophysical Research*, vol. 107, no. A12, 2002. DOI: 10.1029/2002JA009430.
- [20] D. Shepard, "A two-dimensional interpolation for irregularly-spaced data function by," in *23rd ACM National Conference*, 1968. DOI: 10.1145/800186.810616.
- [21] G. P. Styan, "Hadamard products and multivariate statistical analysis," *Linear Algebra and its Applications*, vol. 6, pp. 217-240, 1973. DOI: 10.1016/0024-3795(73)90023-2.
- [22] F. Nielsen, "Hierarchical Clustering," in *Introduction to HPC with MPI for Data Science*, Springer International Publishing, 2016. DOI: 10.1007/978-3-319-21903-5_8, pp. 195-211.
- [23] D. A. Spencer, L. Johnson and A. C. Long, "Solar sailing technology challenges," *Aerospace Science and Technology*, vol. 93, 2019. DOI: 10.1016/j.ast.2019.07.009.